

Speeding up the detectability of the harmonic-space galaxy bispectrum

Francesco Montanari^a and Stefano Camera^{b,c,d}

^aInstituto de Física Teórica IFT-UAM/CSIC, Universidad Autónoma de Madrid, Cantoblanco 28049 Madrid, Spain

^bDipartimento di Fisica, Università degli Studi di Torino, Via P. Giuria 1, 10135 Torino, Italy

^cINFN – Istituto Nazionale di Fisica Nucleare, Sezione di Torino, Via P. Giuria 1, 10135 Torino, Italy

^dINAF – Istituto Nazionale di Astrofisica, Osservatorio Astrofisico di Torino, Strada Osservatorio 20, 10025 Pino Torinese, Italy

E-mail: francesco.montanari@uam.es, stefano.camera@unito.it

Abstract. For the first time we estimate the signal-to-noise ratio (SNR) of the harmonic-space galaxy bispectrum induced by gravity, a complementary probe to Fourier-space clustering analyses. We show how to do it considering only ~ 1000 triangle configurations in multipole space, corresponding to a computational speedup of a factor $\mathcal{O}(10^2) - \mathcal{O}(10^3)$, depending on the redshift bin, when including mildly nonlinear scales. Assuming observational specifications consistent with *Euclid*-like and SKA1-like spectroscopic and photometric galaxy surveys, we show: that given a single redshift bin, spectroscopic surveys outperform photometric surveys by almost an order of magnitude; and that—due to shot-noise and redshift bin width balance—bins at redshifts $z \sim 1$ bring higher cumulative SNR than bins at lower redshifts $z \sim 0.5$. Our results for the cumulative SNR $\lesssim 0.5$ exclude detection of the harmonic-space bispectrum within the single redshift bins here considered and suggest that tomographic studies with upcoming galaxy surveys will be necessary to enhance the detectability. We further discuss how, using the Karhunen-Loève transform, a detection analysis only requires a 1×1 covariance matrix for a single redshift bin.

Contents

1	Introduction	1
2	Tree-level bispectrum and its variance	3
3	Bispectrum geometry in multipole space	5
4	Forecast specifications	7
4.1	Photometric survey	7
4.2	Spectroscopic surveys	8
5	Forecast methodology and results	8
6	Data compression	10
7	Conclusions	12
A	Geometrical factors	13
B	SNR estimate based on interpolation	14
C	Numerical computation	15

1 Introduction

The clustering of galaxies is one of the most important cosmological probes. Hitherto, it has been explored mostly through its two-point statistics, like the galaxy correlation function or the galaxy power spectrum. Both methods have provided excellent constraints on cosmological parameters [e.g., 1–3], soon to be boosted by upcoming surveys that will cover unprecedented volumes and source number densities. In particular, it is worth mentioning: the European Space Agency’s flagship, the *Euclid* satellite [4–7]; the Rubin Observatory (previously known as Large Synoptic Survey Telescope, LSST) [8, 9]; the Dark Energy Survey Experiment [DESI; 10–12]; and the Square Kilometre Array [SKA; 13–18].

On the other hand, due to both a more complex modelling and the limitations of previously available data sets, as well as to high computational requirements, higher-order summary statistics such the bispectrum have played a minor role up to now. However, it is well known that the bispectrum (or its Fourier transform, the 3-point correlation functions) represents a unique window to the primordial Universe [19] and a complementary probe of the large-scale structure (LSS) [20–26].

Often, most studies of galaxy clustering poly-spectra (i.e. power spectrum and beyond) are carried out in Fourier space [27]. However, Fourier-space analyses require a fiducial cosmological model to convert observed angles and redshifts into physical distances and, thus, into Fourier wave-numbers. Instead, the dependence on multipoles and redshifts in harmonic space allows us to perform analyses independent of the dynamics of a specific cosmological model. While the conversion of measurements on the celestial sphere into Fourier modes is typically performed iteratively, and it is controlled by consistency tests, the harmonic- and

Fourier-space estimators are complementary probes and tensions in cosmological parameter constraints obtained with the two methods may be relevant to explain e.g. recent literature results pointing to tensions in determinations of the Universe expansion rate [28]. Furthermore, harmonic-space statistics has a different dependence on some systematic errors than what happens in Fourier space. Hence, here we consider harmonic space clustering analyses not only in view of upcoming photometric galaxy catalogues (for which the relatively poor redshift determination hinders Fourier-space analyses), but also in view of spectroscopic catalogues (typically analysed in Fourier space).

Source number counts have been computed in several perturbation schemes and at different orders in the past (see Ref. [27] for a review in the context of standard perturbation theory). In this work, we rely on the formalism developed in Refs. [29–31] for the tree-level harmonic bispectrum, valid for arbitrary non-interacting dark energy models and modified gravity models provided that photons and dark matter particles move along geodesics. Inclusion of radial selection functions has proven to be computationally challenging even for a simple estimate of the cumulative signal-to-noise ratio (SNR) due to the large number of modes. Here, we provide methodologies to estimate the cumulative SNR using only $\sim 10^3$ multipole configurations, compared to the total $\mathcal{O}(10^5) - \mathcal{O}(10^6)$ available within single redshift bins consistent with upcoming photometric measurements like those performed by *Euclid* or the Rubin Observatory, or spectroscopic observations like for DESI, SKA surveys, or, again, *Euclid*.

Given a methodology for the computation of the theoretical bispectrum, we further discuss a possible strategy for efficient data fit in a detection analysis. Indeed, the covariance matrices needed for the fit can be either computed theoretically (as done here) or estimated from simulations. The latter option is extremely computationally expensive, as the number of simulations needs to be larger than the number of elements of the data vector, which itself is $\mathcal{O}(10^5) - \mathcal{O}(10^6)$ [32]. Oppositely, in our approach the covariance computational runtime is negligible compared to the bispectrum one, but data fitting will still require comparison with simulations to assess the validity of our assumptions. For instance, simulations are necessary to validate the smallest scale included in the analysis. Also, finite volume effects will introduce multipole correlations—here neglected—that in the case of the power spectrum are mitigated via multipole binning validated comparing analytical estimates to simulations [33]. Therefore, we show how to apply the Karhunen-Loève transform (KLT) [34] to the tree-level spherical harmonic bispectrum. The KLT has been used for the Fourier-space bispectrum in [32] to compress information in wave-numbers, and for the harmonic-space power spectrum in [35] to compress radial information in a tomographic analysis involving correlations between several redshift bins. Here, we are rather interested in compressing information in multipoles, since the large number of physical non-vanishing triangular configuration makes it prohibitive to simulate covariance matrices already for a single redshift bin.

In [section 2](#), we review fundamental results for the tree-level harmonic-space bispectrum and its variance. In [section 3](#), we study geometric properties of the bispectrum SNR in multipole space. Forecasts specifications are given in [section 4](#), while the forecast methodology and results are presented in [section 5](#), and [section 6](#) discusses how to reach efficient parameter constraints via the Karhunen-Loève transform. We conclude in [section 7](#). In [Appendix A](#), we list geometrical factors relevant for the bispectrum computation. In [Appendix B](#), we study an alternative forecast methodology as a consistency check for the main analysis. In [Appendix C](#), we give details about the numerical computation of the bispectrum SNR.

Our fiducial cosmology throughout this paper is a flat Λ CDM model with Hubble pa-

parameter, dark matter and baryon density parameters, amplitude, tilt and pivot of the primordial power spectrum given by: $\{h = 0.67, \Omega_{\text{cdm}} = 0.27, \Omega_{\text{b}} = 0.05, A_{\text{s}} = 2.3 \times 10^{-9}, n_{\text{s}} = 0.962, k_{*} = 0.05/\text{Mpc}\}$.

2 Tree-level bispectrum and its variance

We consider the tree-level bispectrum formalism developed in [29–31]. We verified that, given the wide redshift bins considered here, redshift-space distortions and other local terms discussed in [31] are safely negligible. Given that we do not consider correlations among different redshift bins, also integrated terms (e.g. lensing) are negligible for our purposes. Such terms could be relevant for the auto-correlation of a single bin only if this extends over a much larger range $\Delta z \sim \mathcal{O}(1)$ than those of our interest $\Delta z \sim \mathcal{O}(0.1)$ [30]. Hence, for the purposes of our forecasts the bispectrum induced by gravitational nonlinearities is well-approximated by the dominant density contribution.

We assume that source density perturbations are related to matter density perturbations δ via a local bias model, neglecting stochastic bias terms

$$\delta_g = b_1 \delta + \frac{1}{2} b_2 \delta^2 + b_{s^2} s^2. \quad (2.1)$$

We assume the bias coefficients b_1, b_2, b_{s^2} to be scale-independent. The bias coefficient b_{s^2} is related to the tidal field s_{ij} [36] and we defined $s^2 = s_{ij} s^{ij}$. We expand perturbations up to second-order terms $\delta = \delta^{(1)} + \delta^{(2)}$.

The bispectrum of density fluctuations is defined as

$$B^{\delta^{(2)}}(\mathbf{n}_1, \mathbf{n}_2, \mathbf{n}_3, z_1, z_2, z_3) = \left\langle \left\{ b_1(z_1) \delta^{(2)}(\mathbf{n}_1, z_1) + \frac{b_2(z_1)}{2} \left[\delta^{(1)}(\mathbf{n}_1, z_1) \right]^2 + b_{s^2}(z_1) s^2(\mathbf{n}_1, z_1) \right\} \times \left[b_1(z_2) \delta^{(1)}(\mathbf{n}_2, z_2) \right] \left[b_1(z_3) \delta^{(1)}(\mathbf{n}_3, z_3) \right] + \text{cyclic} \right\rangle, \quad (2.2)$$

where cyclic denotes two additional cyclic permutations over the arguments (\mathbf{n}_i, z_i) . These parameters represent the direction of observation $-\mathbf{n}_i$ and the redshift z_i of a given source. The bispectrum can be expanded in spherical harmonics

$$B(\mathbf{n}_1, \mathbf{n}_2, \mathbf{n}_3, z_1, z_2, z_3) = \sum_{\substack{\ell_1, \ell_2, \ell_3 \\ m_1, m_2, m_3}} B_{\ell_1 \ell_2 \ell_3}^{m_1 m_2 m_3}(z_1, z_2, z_3) Y_{\ell_1 m_1}(\mathbf{n}_1) Y_{\ell_2 m_2}(\mathbf{n}_2) Y_{\ell_3 m_3}(\mathbf{n}_3), \quad (2.3)$$

and, using statistical isotropy, the physical information can be further factorised in terms of the reduced bispectrum defined by

$$B_{\ell_1 \ell_2 \ell_3}^{m_1 m_2 m_3}(z_1, z_2, z_3) = \mathcal{G}_{\ell_1 \ell_2 \ell_3}^{m_1 m_2 m_3} b_{\ell_1 \ell_2 \ell_3}(z_1, z_2, z_3). \quad (2.4)$$

In [Appendix A](#) we define the Gaunt integral $\mathcal{G}_{\ell_1 \ell_2 \ell_3}^{m_1 m_2 m_3}$, which is zero unless $m_1 + m_2 + m_3 = 0$ and the following multipole conditions hold:

$$|\ell_2 - \ell_3| \leq \ell_1 \leq \ell_2 + \ell_3 \quad (\text{triangle inequality}), \quad (2.5)$$

$$\ell_1 + \ell_2 + \ell_3 = \text{even}. \quad (2.6)$$

The triangle inequality must be satisfied for all indices permutations.

Using standard cosmological perturbation theory at tree-level, the reduced bispectrum can be written in terms of generalised harmonic power spectra

$${}^n C_{\ell\ell'}(z_1, z_2) = i^{\ell-\ell'} 4\pi \int d \ln k k^n \mathcal{P}_R(k) \Delta_\ell(k, r_1) \Delta_{\ell'}(k, r_2) . \quad (2.7)$$

Here $\mathcal{P}_R(k)$ is the dimensionless power spectrum of primordial curvature perturbations, and we defined $\Delta_\ell(k, r) = T_\delta(k, r) j_\ell(kr)$, where $T_\delta(k, r)$ is the linear transfer function of density perturbations [37], $j_\ell(x)$ is the spherical Bessel function and $r(z)$ is the radial comoving distance to redshift z . The reduced bispectrum reads

$$b_{\ell_1\ell_2\ell_3}^{\delta^{(2)}}(z_1, z_2, z_3) = \left[b_1(z_1) + \frac{21}{34} b_2(z_1) \right] b_{\ell_1\ell_2\ell_3}^{\delta^0}(z_1, z_2, z_3) + b_1(z_1) b_{\ell_1\ell_2\ell_3}^{\delta^1}(z_1, z_2, z_3) \\ + \left[b_1(z_1) + \frac{7}{2} b_{s^2}(z_1) \right] b_{\ell_1\ell_2\ell_3}^{\delta^2}(z_1, z_2, z_3) + \text{O} , \quad (2.8)$$

where we further defined the following contributions

- Monopole:

$$b_{\ell_1\ell_2\ell_3}^{\delta^0}(z_1, z_2, z_3) = \frac{34}{21} C_{\ell_1}(z_1, z_2) C_{\ell_2}(z_1, z_3) . \quad (2.9)$$

- Dipole (the geometrical factors $g_{\ell_1\ell_2\ell_3}$ and $Q_{\ell'\ell''}^{\ell_1\ell_2\ell_3}$ are defined in [Appendix A](#)):

$$b_{\ell_1\ell_2\ell_3}^{\delta^1}(z_1, z_2, z_3) = \frac{(g_{\ell_1\ell_2\ell_3})^{-1}}{16\pi^2} \sum_{\ell'\ell''} (2\ell' + 1)(2\ell'' + 1) Q_1^{\ell_1\ell_2\ell_3} \\ \times \left[{}^1 C_{\ell''\ell_2}(z_1, z_2) {}^{-1} C_{\ell'\ell_3}(z_1, z_3) \right. \\ \left. + {}^{-1} C_{\ell''\ell_2}(z_1, z_2) {}^1 C_{\ell'\ell_3}(z_1, z_3) \right] . \quad (2.10)$$

$Q_1^{\ell_1\ell_2\ell_3}$ is zero unless $\ell' = \ell_2 \pm 1$ and $\ell'' = \ell_1 \pm 1$, hence the imaginary unit factors associated to generalized spectra lead to real results $i^{\ell'+\ell''} (-i)^{\ell_1+\ell_2} = \pm 1$.

- Quadrupole:

$$b_{\ell_1\ell_2\ell_3}^{\delta^2}(z_1, z_2, z_3) = \frac{(g_{\ell_1\ell_2\ell_3})^{-1}}{42\pi^2} \sum_{\ell'\ell''} (2\ell' + 1)(2\ell'' + 1) Q_2^{\ell_1\ell_2\ell_3} \\ \times C_{\ell''\ell_2}(z_1, z_2) C_{\ell'\ell_3}(z_1, z_3) . \quad (2.11)$$

$Q_2^{\ell_1\ell_2\ell_3}$ is zero unless $\ell' = \ell_2 \pm 2, \ell_2$ and $\ell'' = \ell_1 \pm 2, \ell_1$, hence $i^{\ell'+\ell''} (-i)^{\ell_1+\ell_2} = \pm 1$.

The angle-averaged bispectrum (see [Equation A.3](#)) covariance for an arbitrary redshift-dependent angular bispectrum was computed in [31] in the Gaussian approximation $B_{\ell_1\ell_2\ell_3}(z_1, z_2, z_3) \approx 0$. In this case the covariance is diagonal, and the variance for the $\ell_1 + \ell_2 + \ell_3 = \text{even}$ case of our interest is given by

$$\sigma_{B_{\ell_1\ell_2\ell_3}}^2(z_1, z_2, z_3) = C_{\ell_1}^{11} C_{\ell_2}^{22} C_{\ell_3}^{33} + [C_{\ell_1}^{12} C_{\ell_2}^{23} C_{\ell_3}^{31} + C_{\ell_1}^{13} C_{\ell_2}^{21} C_{\ell_3}^{32}] \delta_{\ell_1\ell_2} \delta_{\ell_2\ell_3} \\ + C_{\ell_1}^{11} C_{\ell_2}^{23} C_{\ell_3}^{32} \delta_{\ell_2\ell_3} + C_{\ell_1}^{12} C_{\ell_2}^{21} C_{\ell_3}^{33} \delta_{\ell_1\ell_2} + C_{\ell_1}^{13} C_{\ell_2}^{22} C_{\ell_3}^{31} \delta_{\ell_1\ell_3} . \quad (2.12)$$

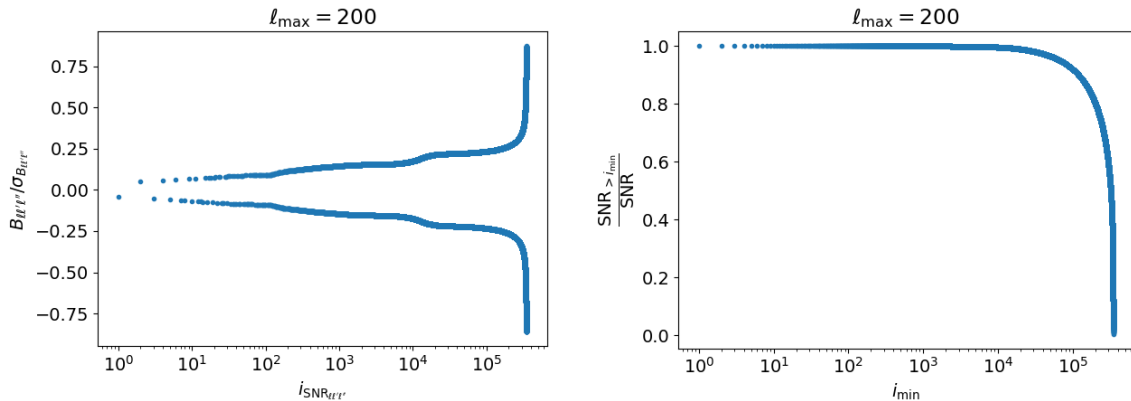


Figure 1. *Left panel:* bispectrum over cosmic variance as function of the i^{th} multipole triangle. Triangles are ordered such that $\text{SNR}_{\ell\ell'\ell''}$ is monotonically sorted. *Right panel:* Fraction of cumulative SNR obtained excluding the first i_{min} triangles.

$\delta_{\ell_i\ell_j}$ is the Kronecker delta and we used the compact notation $C_\ell^{ij} \equiv C_\ell(z_i, z_j) + \epsilon_{ij}$, where we introduced a Poisson shot-noise contribution ϵ_{ij} .

The observable bispectrum and its variance include integration over radial selection functions $\phi_i(z)$:

$$B_{\ell_1\ell_2\ell_3}^{ijk} = \int dz_1 \phi_i(z_1) \int dz_2 \phi_j(z_2) \int dz_3 \phi_k(z_3) B_{\ell_1\ell_2\ell_3}(z_1, z_2, z_3), \quad (2.13)$$

$$\sigma_{B_{\ell_1\ell_2\ell_3}^{ijk}}^2 = \int dz_1 \phi_i(z_1) \int dz_2 \phi_j(z_2) \int dz_3 \phi_k(z_3) \sigma_{B_{\ell_1\ell_2\ell_3}}^2(z_1, z_2, z_3). \quad (2.14)$$

3 Bispectrum geometry in multipole space

To gain insights about geometrical properties of the bispectrum in multipole space, in this section we neglect integration over radial selection functions so that we can compute all the triangle configurations satisfying [Equation 2.5](#), [Equation 2.6](#). We use the convention $3 \leq \ell \leq \ell' \leq \ell'' \leq \ell_{\text{max}} = 200$.¹ We consider the equal redshifts case $z \equiv z_1 = z_2 = z_3 = 0.49$. These specific values of ℓ_{max} and z correspond to the maximum multipole and the mean redshift of our forecast lower photometric redshift bin (see [section 4](#), [section 5](#))—we verified that the picture is qualitatively the same in the range of our interest $z \lesssim 1$, $\ell_{\text{max}} \lesssim 300$. For this configuration we can neglect shot-noise values of the same order of magnitude as those used for our forecasts.

In [Figure 1](#) we show the bispectrum as a function of a given multipole triangle over the respective cosmic variance, $B_{\ell\ell'\ell''}/\sigma_{B_{\ell\ell'\ell''}}$. The index $i_{\text{SNR}_{\ell\ell'\ell''}}$ on the abscissa identifies the triangles ordered to sort $\text{SNR}_{\ell\ell'\ell''} = |B_{\ell\ell'\ell''}|/\sigma_{B_{\ell\ell'\ell''}}$. Let us note that the symmetry around

¹The minimum multipole $\ell_{\text{min}} = 3$ is set by the fact that lower bispectrum multipoles depend on nonlinear terms at the observer.

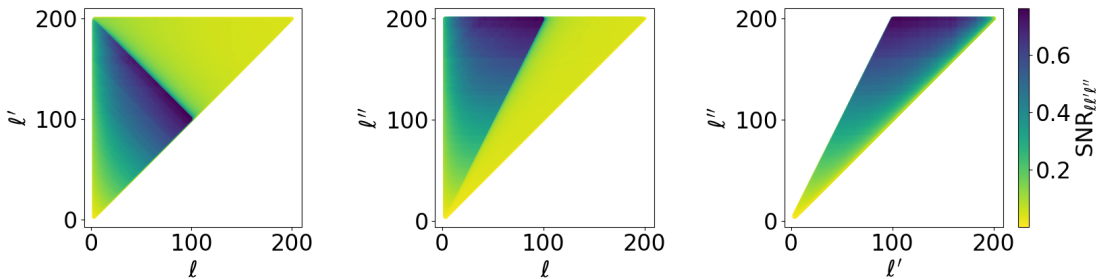


Figure 2. SNR as a function of multipoles. As many points overlap in these two-dimensional projections, we choose to show those with largest $\text{SNR}_{\ell\ell'\ell''}$ for each coordinate combination.

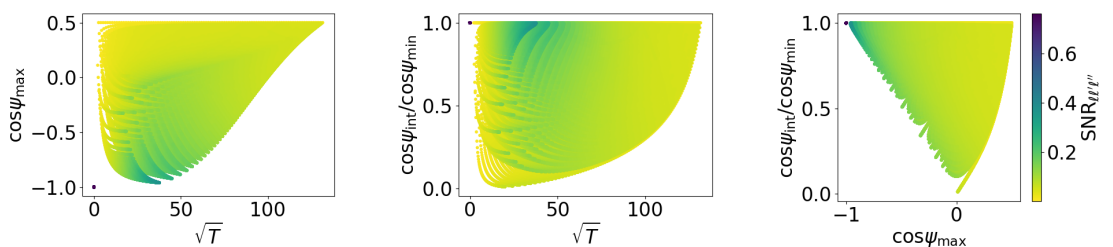


Figure 3. SNR as a function of the square root of the triangle's area \sqrt{T} , of the cosine of the largest internal angle $\cos \psi_{\max}$ and of the ratio between the cosines of the intermediate and smallest angles $\cos \psi_{\text{int}} / \cos \psi_{\min}$.

the abscissa would already allow us to estimate the cumulative SNR^2

$$\text{SNR}(\leq \ell_{\max}) = \sqrt{\sum_{3 \leq \ell \leq \ell' \leq \ell'' \leq \ell_{\max}} \frac{B_{\ell\ell'\ell''}^2}{\sigma_{B_{\ell\ell'\ell''}}^2}} \quad (3.1)$$

considering only about half of the triangles, i.e. only those triangles that lead to a positive bispectrum $(B^+)_{\ell\ell'\ell''}$ as $\text{SNR} \approx \sqrt{2 \sum (B^+)_{\ell\ell'\ell''}^2 / \sigma_{(B^+)_{\ell\ell'\ell''}}^2}$ (similarly, one could consider only negative bispectra) recovering the correct value up to errors $\lesssim 0.1\%$. [Figure 1](#) also shows the cumulative $\text{SNR}_{>i_{\min}}$ obtained excluding the first i_{\min} triangles, relative to the total one. The first triangles $i_{\min} \lesssim 10^3$ do not contribute significantly and could be excluded from the SNR computation. However, in [section 5](#) we will use a more efficient approximation of the cumulative SNR.

[Figure 2](#) shows the SNR per triangle, $\text{SNR}_{\ell\ell'\ell''}$, as a function of multipoles. The largest $\text{SNR}_{\ell\ell'\ell''}$ correspond to $\ell' \approx \ell_{\max} - \ell$, peaking at $\ell = \ell'$, and to $\ell'' \approx 2\ell$ for the largest ℓ'' . Hence, the largest $\text{SNR}_{\ell\ell'\ell''}$ corresponds to the folded configuration $\ell \approx \ell' \approx \ell''/2$. Equilateral configurations $\ell = \ell' = \ell''$ correspond to the minimum $\text{SNR}_{\ell\ell'\ell''}$.³

²We take the sum only over $3 \leq \ell \leq \ell' \leq \ell''$ rather than over $3 \leq \ell, \ell', \ell''$ because the bispectrum is invariant under permutations of multipole indices.

³The apparent sharp transitions from large to small $\text{SNR}_{\ell\ell'\ell''}$ values at $\ell' \approx \ell_{\max} - \ell$ in the $\ell - \ell'$ plane, and at $\ell'' \approx 2\ell$ in the $\ell - \ell''$ are misleading as overlapping points with smaller $\text{SNR}_{\ell\ell'\ell''}$ are not visible in these projections.

As an alternative picture, rather than studying the dependence of $\text{SNR}_{\ell\ell'\ell''}$ on the triangle side lengths, we consider the following coordinates [38]:

- \sqrt{T} , the square root of the triangle's area.
- $\cos \psi_{\max}$, the cosine of the largest internal angle.
- $\cos \psi_{\text{int}} / \cos \psi_{\min}$, the ratio between the cosines of the intermediate and smallest angles.

In Figure 3 several points with large $\text{SNR}_{\ell\ell'\ell''}$ overlap at $\sqrt{T} = 0$, which, given our convention $\ell \leq \ell' \leq \ell''$, correspond to folded triangles $\ell + \ell' = \ell''/2$; the further conditions $\cos \psi_{\max} = -1$ and $\cos \psi_{\text{int}} / \cos \psi_{\min} = 1$ for the largest $\text{SNR}_{\ell\ell'\ell''}$ lead to $\ell \approx \ell' \approx \ell''/2$, as expected. These coordinates make it more clear that equilateral triangles give the smallest $\text{SNR}_{\ell\ell'\ell''}$, as this corresponds to $\cos \psi_{\max} \approx 1/2$ (i.e., $\psi_{\max} \approx 60^\circ$) along all $\sqrt{T} \neq 0$ values, jointly with $\cos \psi_{\text{int}} / \cos \psi_{\min} \approx 1$.

4 Forecast specifications

In this section we outline observable specifications consistent with upcoming galaxy surveys.

4.1 Photometric survey

We consider a photometric *Euclid*-like survey [7]. Radial selection functions can be written as $\phi_i = W_i dN/dz/d\Omega$ [e.g., 39], where the galaxy density per redshift and solid angle is

$$\frac{dN}{dzd\Omega}(z) = \left(\frac{z}{z_0}\right)^2 \exp\left[-\left(\frac{z}{z_0}\right)^{3/2}\right], \quad (4.1)$$

with $z_0 = z_m/\sqrt{2}$ given the mean redshift $z_m = 0.9$, and

$$W_i(z) = \int dz_p P(z_p|z) W_i(z_p). \quad (4.2)$$

We assume a tophat selection $W_i(z_p)$ in photometric redshift space and we take a simple Gaussian form with standard deviation $\sigma_{z,i} = 0.05(1 + \bar{z}_i)$ (\bar{z}_i being the mean photometric redshift within the i th bin) for the probability $P(z_p|z)$ that a galaxy with redshift z has measured redshift z_p . Then the radial selection function is written in terms of the error function as

$$\phi_i(z) \propto \frac{dN}{dzd\Omega} \left(\text{erf} \left[\frac{z_i^+ - z}{\sqrt{2}\sigma_z} \right] - \text{erf} \left[\frac{z_i^- - z}{\sqrt{2}\sigma_z} \right] \right), \quad (4.3)$$

and the normalization constant is set by $\int dz \phi_i(z) = 1$. z_i^- , z_i^+ are the photometric redshifts defining the edges of the i th bin. We consider the following redshift bins, both with surface density of galaxies $\bar{n}_g = 3 \text{ arcmin}^{-2}$ (shot-noise $\epsilon = 1/\bar{n}_g \approx 2.8 \times 10^{-8} \text{ sr}$):

- Low redshift [0.42, 0.56].
- High redshift [0.90, 1.02].

We assume $b_1 = 1.5$ and set the nonlinear coefficients $b_2 \approx -0.69$ and $b_{s^2} \approx -0.14$ according to the fitting formula (based on Λ CDM simulations) [40]

$$b_2 = 0.412 - 2.143 b_1 + 0.929 b_1^2 + 0.008 b_1^3, \quad (4.4)$$

valid in the range $1 \lesssim b_1 \lesssim 9$. We assume Lagrangian local-in-matter-density bias model

$$b_{s^2} = -\frac{2}{7}(b_1 - 1), \quad (4.5)$$

reviewed in [36]. The precise value of the bias coefficients is not relevant for our purposes.

4.2 Spectroscopic surveys

We consider a low-redshift SKA1-like neutral hydrogen galaxy survey and a high-redshift *Euclid*-like spectroscopic survey. Given the good spectroscopic redshift determination, $W_i(z)$ is well approximated by a tophat within the given redshift bins. Also here we consider a low redshift and a high redshift survey, chosen to compare roughly with the photometric survey bins:

- SKA1: $z \in [0.4, 0.6]$, with shot-noise $\epsilon = 1/\bar{n}_g \approx 1.45 \times 10^{-5}$ sr and linear galaxy bias $b_1 \approx 1.02$ consistent with SKA1 Medium-Deep Band 2 Survey (5σ detection threshold) [18, 41]. We use again Equation 4.4 and Equation 4.5 as galaxy bias prescription. Given the smaller redshift range covered than the photometric case, here we neglect the redshift evolution of $dN/dz/d\Omega$ when integrating over selection functions.
- *Euclid*: $z \in [0.9, 1.1]$, with shot-noise $\epsilon = 1/\bar{n}_g \approx 1.68 \times 10^{-7}$ sr consistently with [7], and galaxy bias [25, 31]

$$b_1(z) = 0.9 + 0.4z \quad (4.6)$$

$$b_2(z) = -0.704172 - 0.207993z + 0.183023z^2 - 0.00771288z^3, \quad (4.7)$$

computed at the redshift bin mean \bar{z} . Again, b_{s^2} is given by Equation 4.5. Following [7], also in this case we assume a constant $dN/dz/d\Omega$ when integrating over selection functions.

5 Forecast methodology and results

In this section we forecast bispectrum detection perspectives. Due to our tree-level bispectrum approximation, we only consider mildly nonlinear scales in the following analysis. For the lower redshift bins (mean redshifts $\bar{z} \sim 0.5$) we set ℓ_{\max} values up to $\ell_{\max} = 200$, corresponding to transverse scales of about $r(z = 0.4) \approx 50$ Mpc at our lowest, most nonlinear, redshift bin edge.⁴ For the higher redshift bins ($\bar{z} \sim 1$) we set ℓ_{\max} values up to $\ell_{\max} = 300$, corresponding to $r(z = 0.9) \approx 65$ Mpc at the lowest redshift bin.⁵

⁴We use $r(z) \approx d(z)\theta(\ell)$, where $d(z)$ is the line-of-sight comoving distance and $\theta(\ell) = 2\pi/\ell$ [e.g. 42].

⁵The largest wave number reachable with our perturbative treatment can be estimated as $k_{\max}(z) = 0.1h(1+z)^{2/(2+n_s)}$ [43], giving $\ell_{\max} \approx 170, 370$ at $z \approx 0.5, 1$, respectively. Our $\ell_{\max} = 300$ value at $z \approx 1$ is also set by computational requirements for the case where we evaluate all of the multipoles to test our methodology, as in principle smaller scales could be reached compared to lower redshifts. We don't expect this to affect our conclusions, as our results for $\ell_{\max} = 300$ are already shot-noise limited. It should also be reminded that, due to the different redshifts involved when integrating over selection functions, the correspondence of a given triangle in multipole and configuration space is not trivial. In actual observational analyses, the maximum multipole ℓ_{\max} should be set based on agreement with simulations tailored to the particular survey.

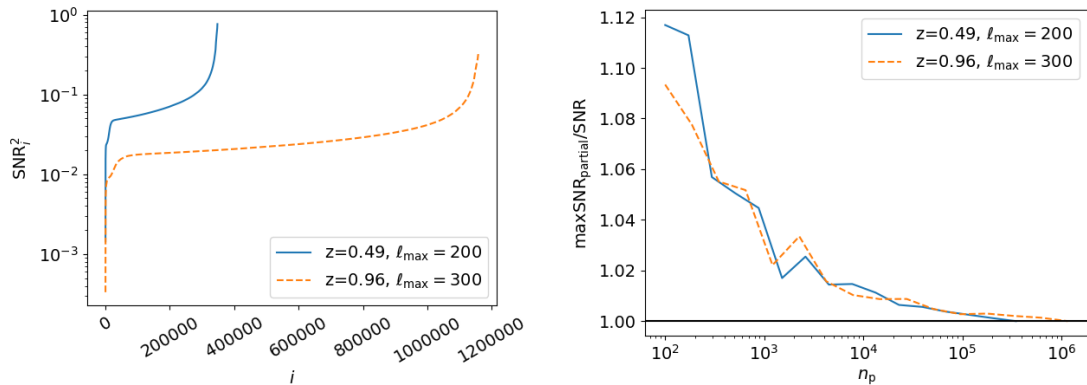


Figure 4. *Left panel:* Sorted SNR for the cases where we neglect radial selection functions. Each index i corresponds to a multipole configuration (ℓ, ℓ', ℓ'') . *Right panel:* We estimate the error induced by approximating the cumulative SNR considering only a partial subset of n_p multipole configurations. For each n_p we consider 100 different random draws from the full set of n_{tot} multipole configurations, and we plot the largest deviation compared to the exact result.

We estimate the cumulative SNR up to ℓ_{max} , given in Equation 3.1. The required number of multipole configurations satisfying Equation 2.5 and Equation 2.6 are 347,755 for $\ell_{\text{max}} = 200$, and 1,157,880 for $\ell_{\text{max}} = 300$. This is computationally prohibitive when including observational selection functions (see Appendix C). Contrary to the case of the power spectrum, where 1-dimensional spline interpolation over one multipole ℓ is routinely used to achieve speedups of a factor 5–10 inducing errors well below $\lesssim 1\%$ [44], 3-dimensional interpolation over the (ℓ, ℓ', ℓ'') multipole triplet is no longer efficient enough. Instead, we approximate

$$\text{SNR}(\leq \ell_{\text{max}}) \approx \sqrt{n_{\text{tot}} \frac{1}{n_p} \sum_{j=1}^{n_p} \left(\frac{B_j^2}{\sigma_{B_j}^2} \right)}, \quad (5.1)$$

where j denotes a given (ℓ, ℓ', ℓ'') multipole configuration. In other words, we approximate the arithmetic mean over all n_{tot} physical configurations with the one over a partial subset of n_p configurations randomly drawn from the total ones. This allows us to recover $\text{SNR}(\leq \ell_{\text{max}})$ at the $\mathcal{O}(1\%)$ level considering only a few ($n_p \sim 10^3$) configurations. We refer the reader to Appendix B, where we compare SNR estimates obtained with a different methodology.

To validate the methodology, we first consider the cases without radial selection functions for which we can compute the cumulative SNR using all the multipole configurations. In Figure 4 we arrange triangle configurations (ℓ, ℓ', ℓ'') to show the sorted SNR. The plot suggests that most configurations have comparable SNR, 1–2 order of magnitudes smaller than the larger SNR. Hence, the cumulative SNR cannot be well approximated considering only the largest SNR configurations (folded multipole triangles, see section 3). However, this also suggests that using only a subsample of triangles to estimate the cumulative SNR is not sensitive to missing large-SNR configurations. In the right panel of Figure 4 we approximate the cumulative SNR as in Equation 5.1. We compute deviations with respect to the non-approximate cumulative SNR considering 100 different random selections of the partial subset of n_p triangles for each n_p and show the largest deviation for each n_p . This gives an estimate of systematic errors introduced by our methodology, mitigating the risk of underestimating

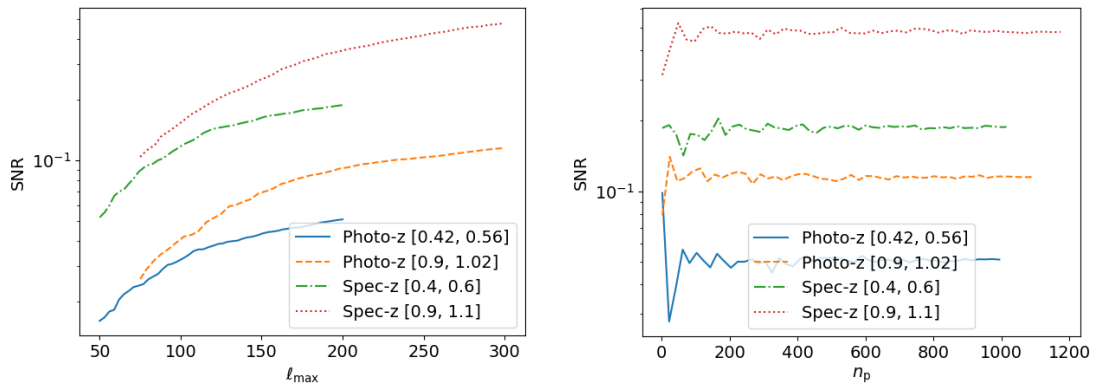


Figure 5. *Left panel:* Cumulative SNR as a function of the maximum multipole for our reference surveys. *Right panel:* Convergence test showing the cumulative SNR as a function of the number of points used to estimate the mean in Equation 5.1.

them due to a particular random draw. We expect to recover the cumulative SNR within $\sim 10\%$ for $n_p \gtrsim 200$, within $\sim 5\%$ for $n_p \gtrsim 10^3$, and within $\sim 1\%$ for $n_p \gtrsim 10^4$.

The cumulative SNR as a function of ℓ_{\max} is shown in Figure 5 for our reference surveys. In each case we consider at least $n_p = 1000$ multipole configurations to estimate Equation 5.1. The curves show small SNR values at small ℓ_{\max} due to cosmic variance, and tend towards a plateau at large ℓ_{\max} where shot-noise is more relevant (however, the necessary inclusion of nonlinearities will likely boost information at the largest ℓ_{\max} , depending on shot-noise counterbalance). The largest SNR are in the range 0.05–0.5, and results show that spectroscopic bins outperform photometric ones. This is due to the fact that large photometric bins significantly smooth and reduce the signal compared to the relatively narrow spectroscopic bins. Furthermore, high mean redshifts $\bar{z} \sim 1.0$ bring larger SNR by about a factor 2 than lower $\bar{z} \sim 0.5$ (despite the fact that we include smaller comoving scales at $\bar{z} \sim 0.5$ due to our choices of ℓ_{\max} dictated by computational limit, as commented in footnote 5). On the one hand, gravitational nonlinearities lead to a larger bispectrum at low redshifts [e.g. 31]. On the other hand, in the spectroscopic case the $\bar{z} \sim 0.5$ bin is affected by a shot-noise 2 orders of magnitude larger than the $\bar{z} \sim 1.0$ bin. In the photometric case both bins have the same shot-noise, but due to the $dN/dz/d\Omega$ distribution this comes at the cost of a significantly larger bin at $\bar{z} \sim 0.5$ than at $\bar{z} \sim 1.0$. As a convergence test, in Figure 5 we also show the cumulative SNR for the largest ℓ_{\max} value in each case, as a function of the number n_p of points used to estimate the mean in Equation 5.1. Results converge within $\sim 1\%$ towards the largest n_p , consistently with the error analysis in Figure 4.

6 Data compression

Here we discuss how to achieve a drastic dimensionality reduction in data fitting analyses using the KLT. Let \mathbf{x} be a Gaussian distributed n -dimensional data vector, and let $\langle \mathbf{x} \rangle$ depend on the m -dimensional parameters vector $\boldsymbol{\theta}$ that we want to constrain. The likelihood and Fisher

matrix are defined by

$$\log \mathcal{L} \propto \frac{1}{2} (\mathbf{x} - \langle \mathbf{x} \rangle)^\top \mathbf{C}^{-1} (\mathbf{x} - \langle \mathbf{x} \rangle), \quad (6.1)$$

$$F_{ij} = \frac{1}{2} \text{Tr} [\mathbf{C}^{-1} \mathbf{C}_{,i} \mathbf{C}^{-1} \mathbf{C}_{,j} + \mathbf{C}^{-1} (\langle \mathbf{x} \rangle_{,i} \langle \mathbf{x} \rangle_{,j}^t + \langle \mathbf{x} \rangle_{,j} \langle \mathbf{x} \rangle_{,i}^t)] , \quad (6.2)$$

The covariance and derivatives entering the Fisher matrix are evaluated at a fiducial cosmology. The KLT is a linear transformation that compresses, without information loss (in the Fisher matrix), the n -dimensional data vector into a m -dimensional one. Then, parameters can be constrained based on a likelihood that depends on the compressed data set, and on a $m \times m$ covariance matrix (rather than the original $n \times n$ one). This dimensionality reduction in the covariance matrix is the main advantage of the KLT (there is no advantage for the computation of the theoretical model). In the case of the bispectrum we expect a large improvement given $m \ll n$.

Let \mathbf{A} be a $m \times n$ transformation matrix, and \mathbf{y} the m -dimensional compressed data vector, i.e.

$$\mathbf{y} = \mathbf{A} \mathbf{x} \quad (6.3)$$

Suppose we are only interested in one parameter, $m = 1$.⁶ Let \mathbf{a}^\top be the only non-vanishing row of the \mathbf{A} matrix. Then, the Fisher matrix has one entry that we label i

$$F_{ii} = \frac{1}{2} \left(\frac{\mathbf{a}^\top \mathbf{C}_{,i} \mathbf{a}}{\mathbf{a}^\top \mathbf{C} \mathbf{a}} \right)^2 + \frac{(\mathbf{a}^\top \langle \mathbf{x} \rangle_{,i})^2}{\mathbf{a}^\top \mathbf{C} \mathbf{a}} . \quad (6.4)$$

We assume the covariance to be weakly dependent on the parameters, such that the first term is negligible compared to the second one. This is an approximation that works well in practical applications [32, 45, 46]. Then, it can be shown analytically [34] that F_{ii} is maximised by

$$\mathbf{a}_i = \mathbf{C}^{-1} \langle \mathbf{x} \rangle_{,i} , \quad (6.5)$$

which gives

$$y_i = \mathbf{a}^\top \langle \mathbf{x} \rangle_{,i} = \langle \mathbf{x} \rangle_{,i}^t \mathbf{C}^{-1} \langle \mathbf{x} \rangle_{,i} . \quad (6.6)$$

Derivatives are taken at a fiducial cosmology.

Inference can be carried out considering the likelihood or Fisher matrix of the compressed data

$$\log \mathcal{L} \propto \frac{1}{2} (\mathbf{y} - \bar{\mathbf{y}})^\top [\mathbf{a}_i^t \mathbf{C} \mathbf{a}_j]^{-1} (\mathbf{y} - \bar{\mathbf{y}}) , \quad (6.7)$$

$$F_{ii} = \langle \mathbf{x} \rangle_{,i}^t \mathbf{C}^{-1} \langle \mathbf{x} \rangle_{,i} . \quad (6.8)$$

The formalism can readily be applied to the bispectrum detection. Our n -dimensional data vector and covariance respectively read

$$\mathbf{x} = \{B_{\ell_1 \ell'_1 \ell''_1}, B_{\ell_2 \ell'_2 \ell''_2}, \dots, B_{\ell_n \ell'_n \ell''_n}\} , \quad (6.9)$$

$$\mathbf{C} = \text{diag} \left(\sigma_{\ell_1 \ell'_1 \ell''_1}^2, \sigma_{\ell_2 \ell'_2 \ell''_2}^2, \dots, \sigma_{\ell_n \ell'_n \ell''_n}^2 \right) . \quad (6.10)$$

A detection analysis can be formalised in terms of constraining the overall amplitude θ of the data $\mathbf{x} = \theta \tilde{\mathbf{x}}$. Then $\langle \mathbf{x} \rangle_{,\theta} = \theta^{-1} \langle \mathbf{x} \rangle$ and our fiducial parameter is $\theta = 1$. At tree-level the bispectrum covariance is computed assuming $\langle B_{\ell \ell' \ell''} \rangle \approx 0$, so it is independent of the amplitude of non-Gaussian coefficients, $\mathbf{C}_{,\theta} \approx 0$. This allows us to estimate the compressed covariance and Fisher matrix as given by Equation 6.7 and Equation 6.8.

⁶To analyse joint constraints on $m > 1$ parameters one can follow the MOPED algorithm [45], or diagonalise the Fisher matrix (e.g. via PCA) before compressing [32].

7 Conclusions

In this work we discussed detection prospects of the gravitational harmonic space bispectrum for upcoming galaxy surveys. We consider mildly nonlinear scales where tree-level standard cosmological theory is valid. First, to get insights about geometrical properties, we studied the dependence of the gravitational bispectrum and its variance on multipole triangles $\ell \leq \ell' \leq \ell''$ when neglecting observational radial selection functions and setting equal redshifts $z = z' = z''$. We showed that the SNR is peaked for folded triangles $\ell = \ell' = \ell''/2$, and minimum for equilateral triangles $\ell = \ell' = \ell''$.

The maximum multipole $\ell_{\max} = 300$ included in the analysis corresponds to $\mathcal{O}(10^6)$ physical multipole triangles. We showed how to estimate the cumulative SNR including observational effects, in particular computationally expensive radial selection functions, based on a partial subset of ~ 1000 multipole configurations. We consider the complementary scenarios of high redshift accuracy, low number density spectroscopic observations and lower redshift accuracy, high number density photometric measurements for cosmological galaxy surveys. As working assumptions, we adopt *Euclid*-like (both spectroscopy and imaging) survey and SKA1-like (line galaxy) survey specifications. Specifically, we study redshift bins with mean redshifts $\bar{z} \sim 0.5$ and $\bar{z} \sim 1$ for a *Euclid*-like photometric survey, compared to a spectroscopic bin at $\bar{z} \sim 0.5$ for a SKA1-like survey, and a bin at $\bar{z} \sim 1$ for a *Euclid*-like spectroscopic survey. We show that, for a given redshift bin, the spectroscopic measurements outperform the photometric ones. Furthermore, bins at $\bar{z} \sim 1$ outperform those at $\bar{z} \sim 0.5$ by about a factor 2. For the spectroscopic surveys this is due to a factor ~ 100 of difference in shot-noise. For the adopted *Euclid* photometric survey specifications, all bins have the same shot-noise, but given the galaxy selection function this implies a much wider redshift bin at $\bar{z} \sim 0.5$ that smooths out and reduces the signal.

Cumulative SNR values range between ~ 0.05 for the photometric cases, and up to ~ 0.5 for the spectroscopic ones. We have neglected partial sky coverage effects, but at first approximation the cumulative SNR scales as $\text{SNR} \rightarrow \sqrt{f_{\text{sky}}} \text{SNR}$ [47], where $f_{\text{sky}} = 0.3, 0.5$ are the sky fractions covered by an *Euclid*-like and SKA1-like survey, respectively. While this suggests that single bin analyses will not reach bispectrum detection, the result is still interesting in view of tomographic studies. For instance, forecasts for the *Euclid* spectroscopic survey expect $n_{\text{bin}} = 5$ redshift bins, and $n_{\text{bin}} = 10$ for the photometric one. In terms of the bispectrum, this would translate into $n_{\text{bin}} \times n_{\text{bin}} \times n_{\text{bin}}$ correlations. The tomographic analysis may also change conclusions about the relative performance of photometric and spectroscopic surveys [42]. The inclusion of redshift cross-correlations may also change the SNR dependence on triangles geometry. Furthermore, surveys that allow fine redshift determination and that are not shot-noise limited, such as 21cm intensity maps, will also benefit from a larger SNR obtained smoothing the signal over much narrower redshift bins, see [47].

We do not use the Limber approximation because for the harmonic bispectrum it is not accurate even at relatively large multipoles [31]. This is computationally requiring given our approach of estimating bispectra via integrations along the line-of-sight. However, the expressions considered here are fully compatible with more computationally efficient power-law expansions [48] that should be considered for future development in this direction. It has been shown that replacing line-of-sight integrals with such an expansion improves runtime up to a factor 400 for the harmonic power spectrum [49], hence presumably even more for the bispectrum. Moreover, when it comes to saving computation time by trimming the number of *cross-bin* correlations, other recent methods can be explored [see 50].

From a data fitting perspective, binning in multipole space should be considered to afford estimating the bispectrum given the large number $\mathcal{O}(10^5) - \mathcal{O}(10^6)$ of multipole configurations here considered. Simulations are needed to validate the nonlinear scale cutoff and the effects of finite survey volume neglected here. Given that estimating covariance matrices from simulations would be computationally prohibitive, we discussed how the Karhunen-Loève transform to compress our n -dimensional data vector into a single parameter, requiring the estimate of a 1×1 covariance. The procedure can be extended to infer multiple parameters [45], and to compress as well radial modes in tomographic analyses [35].

In this work we focused on the bispectrum induced by gravitational evolution, useful to provide complementary constraints on standard cosmological parameters [e.g. 21]. However, the bispectrum is foremost a unique probe of primordial non-Gaussianity. The primordial bispectrum can be comparable to the gravitational one and both of them must be modeled jointly to avoid systematic biases in parameter inference [51]. Inclusion of the primordial bispectrum and a detectability analysis of non-Gaussianity is then an important next step. The forecast methodology outlined here can be applied to the total bispectrum induced by both gravitational nonlinearities and non-Gaussianity.

Acknowledgments

We thank Ruth Durrer, Mona Jalilvand, Rahul Kothari and Roy Maartens for useful discussions. We acknowledge use of the Kerbero cluster at IFT-UAM/CSIC (Madrid, Spain), and the Competence Centre for Scientific Computing (C3S) and use of the OCCAM SuperComputer at Università degli Studi di Torino (Turin, Italy). FM is supported by the Research Project FPA2015-68048-C3-3-P [MINECO-FEDER] and the Centro de Excelencia Severo Ochoa Program SEV-2016-0597. SC acknowledges support from the Italian Ministry of Education, University and Research (MIUR) through the ‘Departments of Excellence 2018-2022’ Grant (L. 232/2016) awarded by MIUR and Rita Levi Montalcini project ‘PROMETHEUS – Probing and Relating Observables with Multi-wavelength Experiments To Help Enlightening the Universe’s Structure’, in the early stages of this project.

A Geometrical factors

In this section we define geometrical quantities entering the computation of the tree-level bispectrum, see [section 2](#).

The Gaunt integral is defined by

$$\begin{aligned} \mathcal{G}_{\ell_1 \ell_2 \ell_3}^{m_1 m_2 m_3} &= \int d\Omega_{\mathbf{n}} Y_{\ell_1 m_1}(\mathbf{n}) Y_{\ell_2 m_2}(\mathbf{n}) Y_{\ell_3 m_3}(\mathbf{n}) \\ &= \begin{pmatrix} \ell_1 & \ell_2 & \ell_3 \\ 0 & 0 & 0 \end{pmatrix} \begin{pmatrix} \ell_1 & \ell_2 & \ell_3 \\ m_1 & m_2 & m_3 \end{pmatrix} \sqrt{\frac{(2\ell_1 + 1)(2\ell_2 + 1)(2\ell_3 + 1)}{4\pi}}, \end{aligned} \quad (\text{A.1})$$

where $\Omega_{\mathbf{n}}$ is the solid angle spanned by \mathbf{n} and we introduced Wigner’s 3-j symbols. The Gaunt integral satisfies the symmetries discussed in [Equation 2.5](#) and [Equation 2.6](#) and the paragraph above them. The factor

$$g_{\ell_1 \ell_2 \ell_3} = \sqrt{\frac{(2\ell_1 + 1)(2\ell_2 + 1)(2\ell_3 + 1)}{4\pi}} \begin{pmatrix} \ell_1 & \ell_2 & \ell_3 \\ 0 & 0 & 0 \end{pmatrix} \quad (\text{A.2})$$

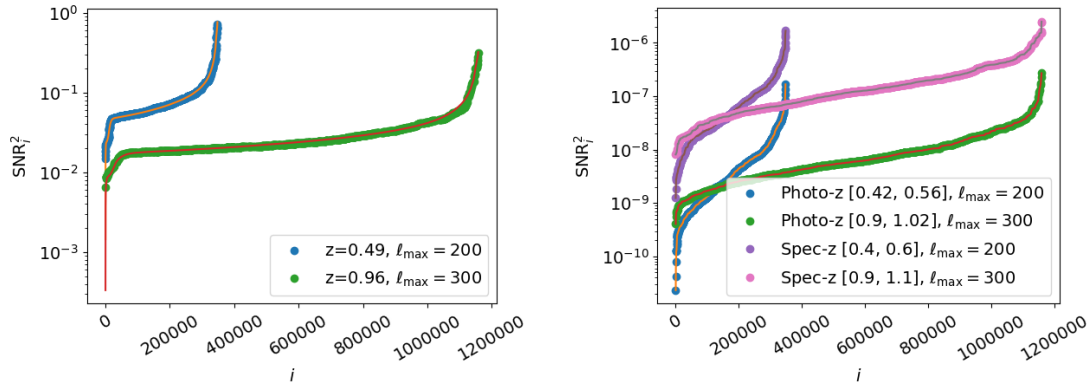


Figure 6. *Left panel:* SNR for a random selection of 10^3 multipole configurations uniformly distributed along the whole range as described in the text. Solid lines show the full result for the cases that neglect radial selection functions. *Right panel:* SNR per multipole configuration including our survey forecast specifications. Solid lines show the interpolating function.

relates the reduced bispectrum to the angle-averaged one

$$\begin{aligned}
 g_{\ell_1 \ell_2 \ell_3} b_{\ell_1 \ell_2 \ell_3}(z_1, z_2, z_3) &= \sum_{m_1, m_2, m_3} \begin{pmatrix} \ell_1 & \ell_2 & \ell_3 \\ m_1 & m_2 & m_3 \end{pmatrix} B_{\ell_1 \ell_2 \ell_3}^{m_1 m_2 m_3}(z_1, z_2, z_3) \\
 &= B_{\ell_1 \ell_2 \ell_3}(z_1, z_2, z_3).
 \end{aligned} \tag{A.3}$$

The factor

$$Q_{\ell \ell' \ell''}^{\ell_1 \ell_2 \ell_3} = I_{\ell \ell' \ell''}^{\ell_1 \ell_2 \ell_3} \begin{Bmatrix} \ell_1 & \ell_2 & \ell_3 \\ \ell' & \ell'' & \ell \end{Bmatrix} (-1)^{\ell + \ell' + \ell''}, \tag{A.4}$$

is expressed in terms of Wigner's 6-j symbols and of

$$I_{\ell \ell' \ell''}^{\ell_1 \ell_2 \ell_3} \equiv \sqrt{(4\pi)^3 (2\ell_1 + 1)(2\ell_2 + 1)(2\ell_3 + 1)} \begin{pmatrix} \ell & \ell'' & \ell_1 \\ 0 & 0 & 0 \end{pmatrix} \begin{pmatrix} \ell' & \ell & \ell_2 \\ 0 & 0 & 0 \end{pmatrix} \begin{pmatrix} \ell'' & \ell' & \ell_3 \\ 0 & 0 & 0 \end{pmatrix}. \tag{A.5}$$

Typically, using Wigner's symbols symmetries, only a few coefficients of $Q_{\ell \ell' \ell''}^{\ell_1 \ell_2 \ell_3}$ are non-vanishing for a given ℓ .

B SNR estimate based on interpolation

Here we discuss an alternative method to Equation 5.1 to approximate the cumulative SNR using only a partial subset of n_p multipole configurations. We use the fact that the $\text{SNR}_{\ell \ell' \ell''}^2$ can be monotonically sorted as discussed in section 3: we map triplets (ℓ, ℓ', ℓ'') to an index i whose order sorts $\text{SNR}_{\ell \ell' \ell''}$ (see Figure 4). Then, we compute $\text{SNR}_{\ell \ell' \ell''}^2$ for n_p randomly selected (ℓ, ℓ', ℓ'') triangle configurations. To sum over all triangles contributing to the cumulative SNR, we distribute uniformly the selected configurations over the whole index i range and interpolate. More precisely, we draw $n_p - 2$ random integers from a uniform distribution within the open interval $(1, n_{\text{tot}})$, where n_{tot} is the total number of physical multipole triangles corresponding to ℓ_{max} , and include the boundaries $i = 1, n_t$.

This method is illustrated in Figure 6. In the left panel we compare the full result for the cases without selection function to a random selection of 10^3 interpolating configurations. The

Configuration	Runtime
No $\phi(z)$	0.3 s
Photometric	60 min
Spectroscopic	20 min

Table 1. Average runtime required to compute the SNR for one multipole triangle configuration using 8 CPUs of an Intel Xeon CPU E5506 @ 2.13GHz processor. We include the cases without integration over selection functions $\phi(z)$, the photometric and spectroscopic redshift bins of our forecasts.

tails of SNR_i are the most critical features driving sampling requirements, together with the fact that SNR_i spans 2–3 order of magnitude. We checked that linear and cubic interpolations agree well, hence we opt for the simpler linear one. We verified that this method agrees well with the one described in the main section, leading to similar intrinsic systematic errors (see right panel of [Figure 4](#)).

The right panel of [Figure 6](#) shows the SNR_i^2 interpolation results for our reference surveys. For each case we consider at least $n_{\text{int}} = 1000$. The functional dependence on the sorting index i is similar to case without selection function, hence we expect to recover the cumulative SNR within 5% errors. Results are consistent with [Figure 5](#).

C Numerical computation

For the numerical computation of the bispectrum and its covariance we use a modified version of the C++ backend of the Python-based Byspectrum code originally developed in [\[31\]](#). Cosmological transfer functions are computed using CLASS [\[44\]](#). We use the Suave algorithm of the Cuba library [\[52\]](#) to perform integrals over radial selection functions,⁷ and the WIGXJPF library [\[53\]](#) to compute Wigner symbols required for the geometric terms defined in [Appendix A](#).

In [table 1](#) we report the average runtime to compute $\text{SNR}_{\ell\ell'\ell''}$ for one multipole triangle configuration for the different cases studied in this work, relative to one node of a computer cluster.⁸ This table is only meant to provide an indicative order of magnitude. We stress that runtime is not homogeneous across all triangle configurations and, as described in [section 5](#), the cases at larger mean redshifts $\bar{z} \sim 1$ reach larger multipole values $\ell_{\text{max}} = 300$, compared to $\ell_{\text{max}} = 200$ at lower redshifts $\bar{z} \sim 0.5$. The different ℓ_{max} is the main reason why, for each separate case reported in [table 1](#), computations at higher redshifts can take up to 10% longer than lower redshifts. Also, the scaling with the number of CPUs (within a single node) is not linear, hence we report the runtime relative to all of the CPUs used. In the cases without selection functions we compute the bispectrum for different multipole triangles in parallel with OpenMP.⁹ When including selection functions, bispectra at different multipole triangles are computed serially in a given node, but numerical integrals are carried out in parallel as detailed above. In this case, the parallel computation scheme [\[54\]](#) does not lead to optimal CPU loading. Furthermore, we consider a single set of numerical precision parameters set to reach convergence for all cases, while each redshift bin could be optimised separately leading to considerable speedup. However, rather than improving on these aspects, we deem it more

⁷We verified that trilinear interpolation of the integrand over the redshift grid (z_1, z_2, z_3) , see [Equation 2.13](#), is not efficient enough to bring significant improvements.

⁸Given the independence of the bispectrum at different multipole triangles, the computation can be further distributed over several nodes of the cluster.

⁹<https://www.openmp.org/>

promising to first pursue the power-law expansion mentioned in [section 7](#) to significantly reduce runtime.

References

- [1] DES collaboration, *Dark Energy Survey year 1 results: Cosmological constraints from galaxy clustering and weak lensing*, *Phys. Rev. D* **98** (2018) 043526 [[1708.01530](#)].
- [2] DES collaboration, *Dark Energy Survey Year 1 Results: Measurement of the Galaxy Angular Power Spectrum*, *Mon. Not. Roy. Astron. Soc.* **487** (2019) 3870 [[1807.10163](#)].
- [3] EBOSS collaboration, *The Completed SDSS-IV extended Baryon Oscillation Spectroscopic Survey: Cosmological Implications from two Decades of Spectroscopic Surveys at the Apache Point observatory*, [2007.08991](#).
- [4] EUCLID collaboration, *Euclid Definition Study Report*, *ESA-SRE* **12** (2011) [[1110.3193](#)].
- [5] EUCLID THEORY WORKING GROUP collaboration, *Cosmology and fundamental physics with the Euclid satellite*, *Living Rev. Rel.* **16** (2013) 6 [[1206.1225](#)].
- [6] EUCLID THEORY WORKING GROUP collaboration, *Cosmology and fundamental physics with the Euclid satellite*, *Living Rev. Rel.* **21** (2018) 2 [[1606.00180](#)].
- [7] EUCLID collaboration, *Euclid preparation: VII. Forecast validation for Euclid cosmological probes*, *eprint* (2019) [[1910.09273](#)].
- [8] Z. Ivezić, J. Tyson, R. Allsman, J. Andrew, R. Angel et al., *LSST: from Science Drivers to Reference Design and Anticipated Data Products*, [0805.2366](#).
- [9] LSST Dark Energy Science Collaboration, *Large Synoptic Survey Telescope: Dark Energy Science Collaboration*, *ArXiv e-prints* (2012) [[1211.0310](#)].
- [10] DESI collaboration, *The Dark Energy Spectroscopic Instrument (DESI)*, *Proc. SPIE Int. Soc. Opt. Eng.* **9147** (2014) 91470S.
- [11] DESI collaboration, *The DESI Experiment Part I: Science, Targeting, and Survey Design*, [1611.00036](#).
- [12] DESI collaboration, *The Dark Energy Spectroscopic Instrument (DESI)*, [1907.10688](#).
- [13] SKA COSMOLOGY SWG collaboration, *Overview of Cosmology with the SKA*, *PoS AASKA14* (2015) 016 [[1501.04076](#)].
- [14] P. Bull, S. Camera, A. Raccanelli, C. Blake, P. Ferreira, M. Santos et al., *Measuring baryon acoustic oscillations with future SKA surveys*, *PoS AASKA14* (2015) 024.
- [15] A. Raccanelli, P. Bull, S. Camera, C. Blake, P. Ferreira et al., *Measuring redshift-space distortion with future SKA surveys*, *PoS AASKA14* (2015) 031.
- [16] F. B. Abdalla, P. Bull, S. Camera, A. Benoit-Lévy, B. Joachimi et al., *Cosmology from HI galaxy surveys with the SKA*, *PoS AASKA14* (2015) 017.
- [17] M. Santos, P. Bull, D. Alonso, S. Camera, P. Ferreira et al., *Cosmology from a SKA HI intensity mapping survey*, *PoS AASKA14* (2015) 019.
- [18] SKA COSMOLOGY SWG collaboration, *Cosmology with Phase 1 of the Square Kilometre Array: Red Book 2018: Technical specifications and performance forecasts*, *Submitted to: Publ. Astron. Soc. Austral.* (2018) [[1811.02743](#)].
- [19] M. Celoria and S. Matarrese, *Primordial Non-Gaussianity*, **12**, 2018, [1812.08197](#).
- [20] H. Gil-Marín, J. Noreña, L. Verde, W. J. Percival, C. Wagner, M. Manera et al., *The power spectrum and bispectrum of SDSS DR11 BOSS galaxies - I. Bias and gravity*, *Mon. Not. R. Astron. Soc.* **451** (2015) 539 [[1407.5668](#)].

- [21] H. Gil-Marín, W. J. Percival, L. Verde, J. R. Brownstein, C.-H. Chuang, F.-S. Kitaura et al., *The clustering of galaxies in the SDSS-III Baryon Oscillation Spectroscopic Survey: RSD measurement from the power spectrum and bispectrum of the DR12 BOSS galaxies*, *Mon. Not. Roy. Astron. Soc.* **465** (2017) 1757 [[1606.00439](#)].
- [22] Z. Slepian, D. J. Eisenstein, J. R. Brownstein, C.-H. Chuang, H. Gil-Marín, S. Ho et al., *Detection of baryon acoustic oscillation features in the large-scale three-point correlation function of SDSS BOSS DR12 CMASS galaxies*, *Mon. Not. R. Astron. Soc.* **469** (2017) 1738 [[1607.06097](#)].
- [23] Z. Slepian, D. J. Eisenstein, F. Beutler, C.-H. Chuang, A. J. Cuesta, J. Ge et al., *The large-scale three-point correlation function of the SDSS BOSS DR12 CMASS galaxies*, *Mon. Not. R. Astron. Soc.* **468** (2017) 1070.
- [24] D. W. Pearson and L. Samushia, *A Detection of the Baryon Acoustic Oscillation features in the SDSS BOSS DR12 Galaxy Bispectrum*, *Mon. Not. R. Astron. Soc.* **478** (2018) 4500 [[1712.04970](#)].
- [25] V. Yankelevich and C. Porciani, *Cosmological information in the redshift-space bispectrum*, *Mon. Not. Roy. Astron. Soc.* **483** (2019) 2078 [[1807.07076](#)].
- [26] M. Rizzato, K. Benabed, F. Bernardeau and F. Lacasa, *Tomographic weak lensing bispectrum: a thorough analysis towards the next generation of galaxy surveys*, *Mon. Not. Roy. Astron. Soc.* **490** (2019) 4688 [[1812.07437](#)].
- [27] F. Bernardeau, S. Colombi, E. Gaztanaga and R. Scoccimarro, *Large scale structure of the universe and cosmological perturbation theory*, *Phys. Rept.* **367** (2002) 1 [[astro-ph/0112551](#)].
- [28] D. Camarena and V. Marra, *A new method to build the (inverse) distance ladder*, [1910.14125](#).
- [29] E. Di Dio, R. Durrer, G. Marozzi and F. Montanari, *Galaxy number counts to second order and their bispectrum*, *JCAP* **1412** (2014) 017 [[1407.0376](#)].
- [30] E. Di Dio, R. Durrer, G. Marozzi and F. Montanari, *The bispectrum of relativistic galaxy number counts*, *JCAP* **1601** (2016) 016 [[1510.04202](#)].
- [31] E. Di Dio, R. Durrer, R. Maartens, F. Montanari and O. Umeh, *The Full-Sky Angular Bispectrum in Redshift Space*, *JCAP* **1904** (2019) 053 [[1812.09297](#)].
- [32] D. Gualdi, M. Manera, B. Joachimi and O. Lahav, *Maximal compression of the redshift space galaxy power spectrum and bispectrum*, *Mon. Not. Roy. Astron. Soc.* **476** (2018) 4045 [[1709.03600](#)].
- [33] A. Cabre, P. Fosalba, E. Gaztanaga and M. Manera, *Error analysis in cross-correlation of sky maps: Application to the ISW detection*, *Mon. Not. Roy. Astron. Soc.* **381** (2007) 1347 [[astro-ph/0701393](#)].
- [34] M. Tegmark, A. Taylor and A. Heavens, *Karhunen-Loeve eigenvalue problems in cosmology: How should we tackle large data sets?*, *Astrophys. J.* **480** (1997) 22 [[astro-ph/9603021](#)].
- [35] D. Alonso, *Science-driven 3D data compression*, *Mon. Not. Roy. Astron. Soc.* **473** (2018) 4306 [[1707.08950](#)].
- [36] V. Desjacques, D. Jeong and F. Schmidt, *Large-Scale Galaxy Bias*, *Phys. Rept.* **733** (2018) 1 [[1611.09787](#)].
- [37] E. Di Dio, F. Montanari, J. Lesgourgues and R. Durrer, *The CLASSgal code for Relativistic Cosmological Large Scale Structure*, *JCAP* **1311** (2013) 044 [[1307.1459](#)].
- [38] D. Gualdi, H. Gil-Marín, M. Manera, B. Joachimi and O. Lahav, *GEOMAX: beyond linear compression for 3pt galaxy clustering statistics*, [1912.01011](#).
- [39] J. Asorey, M. Crocce, E. Gaztañaga and A. Lewis, *Recovering 3D clustering information with angular correlations*, *Mon. Not. R. Astron. Soc.* **427** (2012) 1891 [[1207.6487](#)].

- [40] T. Lazeyras, C. Wagner, T. Baldauf and F. Schmidt, *Precision measurement of the local bias of dark matter halos*, *JCAP* **1602** (2016) 018 [[1511.01096](#)].
- [41] K. Tanidis and S. Camera, *Developing a unified pipeline for large-scale structure data analysis with angular power spectra – I. The importance of redshift-space distortions for galaxy number counts*, *Mon. Not. Roy. Astron. Soc.* **489** (2019) 3385 [[1902.07226](#)].
- [42] E. Di Dio, F. Montanari, R. Durrer and J. Lesgourgues, *Cosmological Parameter Estimation with Large Scale Structure Observations*, *JCAP* **01** (2014) 042 [[1308.6186](#)].
- [43] R. Maartens, S. Jolicoeur, O. Umeh, E. M. De Weerd, C. Clarkson and S. Camera, *Detecting the relativistic galaxy bispectrum*, *JCAP* **03** (2020) 065 [[1911.02398](#)].
- [44] D. Blas, J. Lesgourgues and T. Tram, *The Cosmic Linear Anisotropy Solving System (CLASS) II: Approximation schemes*, *JCAP* **1107** (2011) 034 [[1104.2933](#)].
- [45] A. Heavens, R. Jimenez and O. Lahav, *Massive lossless data compression and multiple parameter estimation from galaxy spectra*, *Mon. Not. Roy. Astron. Soc.* **317** (2000) 965 [[astro-ph/9911102](#)].
- [46] A. Heavens, E. Sellentin, D. de Mijolla and A. Vianello, *Massive data compression for parameter-dependent covariance matrices*, *Mon. Not. Roy. Astron. Soc.* **472** (2017) 4244 [[1707.06529](#)].
- [47] R. Durrer, M. Jalilvand, R. Kothari, R. Maartens and F. Montanari, *Full-sky bispectrum in redshift space for 21cm intensity maps*, [2008.02266](#).
- [48] V. Assassi, M. Simonović and M. Zaldarriaga, *Efficient evaluation of angular power spectra and bispectra*, *JCAP* **1711** (2017) 054 [[1705.05022](#)].
- [49] N. Schöneberg, M. Simonović, J. Lesgourgues and M. Zaldarriaga, *Beyond the traditional Line-of-Sight approach of cosmological angular statistics*, *JCAP* **1810** (2018) 047 [[1807.09540](#)].
- [50] S. Camera, J. Fonseca, R. Maartens and M. G. Santos, *Optimized angular power spectra for spectroscopic galaxy surveys*, *Mon. Not. Roy. Astron. Soc.* **481** (2018) 1251 [[1803.10773](#)].
- [51] E. Di Dio, H. Perrier, R. Durrer, G. Marozzi, A. Moradinezhad Dizgah, J. Noreña et al., *Non-Gaussianities due to Relativistic Corrections to the Observed Galaxy Bispectrum*, *JCAP* **1703** (2017) 006 [[1611.03720](#)].
- [52] T. Hahn, *CUBA: A Library for multidimensional numerical integration*, *Comput. Phys. Commun.* **168** (2005) 78 [[hep-ph/0404043](#)].
- [53] H. T. Johansson and C. Forssén, *Fast and accurate evaluation of Wigner 3j, 6j, and 9j symbols using prime factorisation and multi-word integer arithmetic*, *SIAM J. Sci. Statist. Comput.* **38** (2016) A376 [[1504.08329](#)].
- [54] T. Hahn, *Concurrent Cuba*, *J. Phys. Conf. Ser.* **608** (2015) 012066 [[1408.6373](#)].